



Universiteit
Leiden
The Netherlands

Molecular fingerprints of star formation throughout the Universe : a space-based infrared study

Lahuis, F.

Citation

Lahuis, F. (2007, May 9). *Molecular fingerprints of star formation throughout the Universe : a space-based infrared study*. Retrieved from <https://hdl.handle.net/1887/11950>

Version: Corrected Publisher's Version

License: [Licence agreement concerning inclusion of doctoral thesis in the Institutional Repository of the University of Leiden](#)

Downloaded from: <https://hdl.handle.net/1887/11950>

Note: To cite this publication please use the final published version (if applicable).

Chapter 6

c2d *Spitzer* IRS Spectra of Embedded Protostars: Gas-phase Lines

Abstract

We present a survey of mid-infrared pure rotational H₂ and atomic fine structure lines toward a sample of 56 young stellar objects. The sample consists of low-mass embedded protostars and edge-on disks around pre-main sequence stars selected from the *Spitzer* "From Molecular Cores to Planet Forming Disks" (c2d) legacy program on the basis of silicate absorption at 10 μm. Both spatially unresolved and extended emission is observed. The extended component on scales of several thousand AU is dominated by the [Si II] line and warm ($\lesssim 700$ K) H₂ emission observed in the H₂ S(1) and S(2) lines. The extended emission is shown to be consistent with a photodissociation region (PDR) in the beam. The extended PDR emission is mostly observed toward sources with a low apparent optical depth of the 9.8 μm silicate band. This suggests that the PDRs exist in a thin envelope heated by the central star or that the PDRs are heated by the external radiation field which influences the envelope characteristics. Hot H₂ emission ($T_{\text{ex}} \gtrsim 500$ K) and emission from [Ne II] 12.8 μm, [Fe I] 24 μm, [Fe II] 18 μm, and [S I] 25.2 μm is observed mostly toward the compact source component, and most likely results from shocked gas close to the central star. For three sources excitation temperatures of $\sim 1300 - 1500$ K and gas masses of $\sim (0.2 - 1) \times 10^{-3} M_{\text{J}}$ are derived, putting an upper on the size of the emitting region of $r \lesssim 50$ AU.

Lahuis, F., van Dishoeck, E. F., Jørgensen, J. K., Blake, G. A., Evans, II, N. J 2007, in preparation

6.1 Introduction

The interstellar medium (ISM) surrounding forming stars is subject to highly energetic processes. Strong ultraviolet (UV) radiation heats the ISM to form a photon-dominated or photodissociation region (PDR) (Hollenbach et al., 1991; Hollenbach & Tielens, 1999). In the PDR layer closest to the star most molecular material is dissociated and the atomic species are ionized resulting in fine structure lines such as [OI], [Fe I], and [SI]. Further out H₂ is excited and the lower pure rotational H₂ lines become strong (e.g. Kaufman et al., 2006, applied to regions of massive star formation).

The young accreting stars produce strong stellar and/or disk winds generating a bipolar outflow cavity and entraining material. The winds impact onto the surrounding material producing supersonic shock fronts that compress and heat the gas. Two types of shocks are identified, low velocity continuous shocks, *C*-shocks, and high velocity discontinuous or ‘jump’ shocks, *J*-shocks (Hollenbach, 1997; Walmsley et al., 2005).

Low velocity shocks ($v_s \lesssim 40 \text{ km s}^{-1}$) compress the ionized material and magnetic fields ahead of the shock. The gas can be heated up to $\sim 1000 \text{ K}$ and most of the cooling is through molecular lines (e.g. Neufeld & Kaufman, 1993; Kaufman, 1995). In high velocity shocks ($v_s \gtrsim 40 \text{ km s}^{-1}$) the neutral pre-shock gas is heated through viscous heating in a thin shock front in which radiative cooling is weak. The post-shock gas can be heated up to $\sim 10,000 \text{ K}$ in which most of the molecular material is dissociated and a large fraction of the atoms are ionized resulting in strong emission lines of singly and doubly ionized atoms. Further downstream from the shock hydrogen recombines in the cooled down gas and strong emission of high-*J* pure rotational lines are expected (Hollenbach & McKee, 1989).

So far, PDRs and shocks have mostly been studied in the general ISM near massive young stars or supernova remnants. Previous observations of low mass young stars using ground-based instruments or the ISO-SWS instrument (de Graauw et al., 1996; van den Ancker, 1999) either lacked the sensitivity or spatial resolution to separate the various emitting regions. The sensitive InfraRed Spectrograph (IRS) (Houck et al., 2004) on board the *Spitzer* Space Telescope (Werner et al., 2004) brings the detection of the mid-IR H₂ pure rotational and atomic fine structure lines within reach for young solar mass stars in nearby star forming regions. The combination of high sensitivity, moderate spectral resolution $R = \lambda/\Delta\lambda = 600$, and modest spatial resolution makes *Spitzer* well suited for the study of the gas in the ISM around low-mass young stars in nearby ($\lesssim 300 \text{ pc}$) clouds. These lines can help to identify the heating processes, PDR or shock-driven, taking place.

A general complication in the interpretation of emission from the environments of young embedded stars are contributions from multiple unrelated processes along the line of sight. In particular emission of the extended (remnant) envelope on scales of 10,000 AU and the small inner envelope near the young star on scales of $< 1000 \text{ AU}$ trace completely distinct physical processes. The *Spitzer* IRS beam in principle makes it possible to resolve structures up to $\sim 1000 \text{ AU}$ in size for nearby star forming regions at distances up to a few hundred pc. However, the IRS full-slit extraction for the high resolution echelle modules and the fixed-width extraction for the low resolution long-slit modules do not allow a separation of extended envelope and small-scale emission.

We present here an overview of the mid-IR gas-phase lines detected in embedded sources and edge-on circumstellar disks observed in the *Spitzer* legacy program “From Molecular Cores to Planet Forming Disks” (“Cores to Disks” or c2d) (Evans

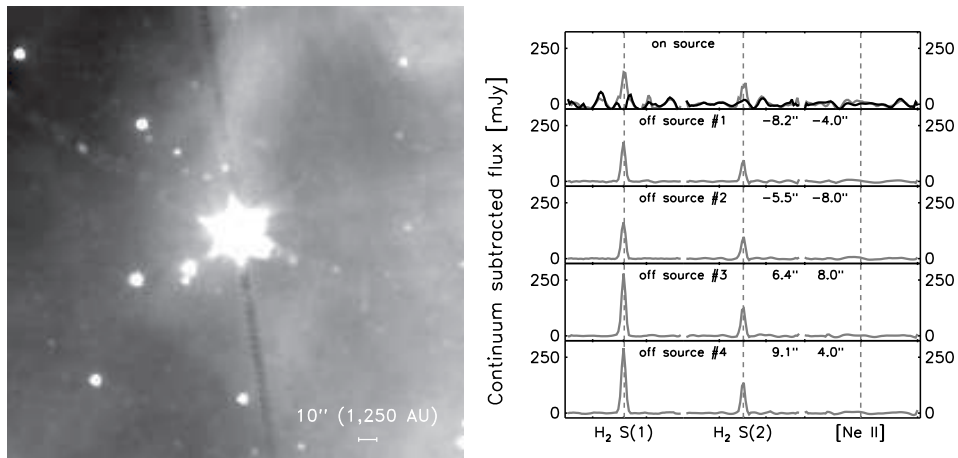


Figure 6.1 SH minimap observed around VSSG1 in Ophiuchus. The left plot displays an IRAC image at $4.5 \mu\text{m}$ (including the high excitation H_2 S(9), S(10) and S(11) lines) showing the star plus diffuse extended emission. The right plot shows the observed emission of the on-source observation (top panel) and the off-source observations from the minimap. In gray the total observed emission and in black the unresolved source emission toward VSSG1.

et al., 2003), which has collected a large sample of IRS spectra toward sources in the nearby Chamaeleon, Lupus, Perseus, Ophiuchus, and Serpens star-forming regions. High-S/N spectra have been obtained within the $5 - 38 \mu\text{m}$ range for 226 sources at all phases of star and planet formation up to ages of ~ 5 Myr. The observations presented in this chapter show the results of an optimal extraction method, developed by the c2d team, which does allow the separation of both spatial components within the IRS aperture. We will demonstrate the importance of being able to do so for the study of young embedded objects. In Section 6.2 the source selection and data reduction are explained. In Section 6.3 the observed atomic fine-structure and H_2 emission lines and the derived parameters are presented. In Section 6.4 the results are reviewed in the context of PDR and shock heating.

6.2 Observations and data reduction

A description of the c2d program is included in §3.1 and §5.2. The 56 sources presented in this chapter were all selected for showing the $10 \mu\text{m}$ silicate band in absorption. This criterion includes embedded Class 0 and Class I sources plus edge-on disk (Class II) sources ($i \gtrsim 65$ degrees) which were excluded from the gas-disk study presented in Lahuis et al. (2007) such as CRBR 2422.8-3423 (Pontoppidan et al., 2005) and IRS 46 (Lahuis et al., 2006b). The selected sources are listed in Table 6.1 which gives the basic observing and source parameters and the adopted distances. Note that in most cases, it is not possible to determine whether the infrared source is dominated by an envelope or a disk without spatially resolved infrared or (sub)millimeter data. Known or candidate edge-on disks are labeled in the table. Even though the majority of the remaining sources are thought to be embedded protostars, there may be additional cases dominated by an edge-on disk.

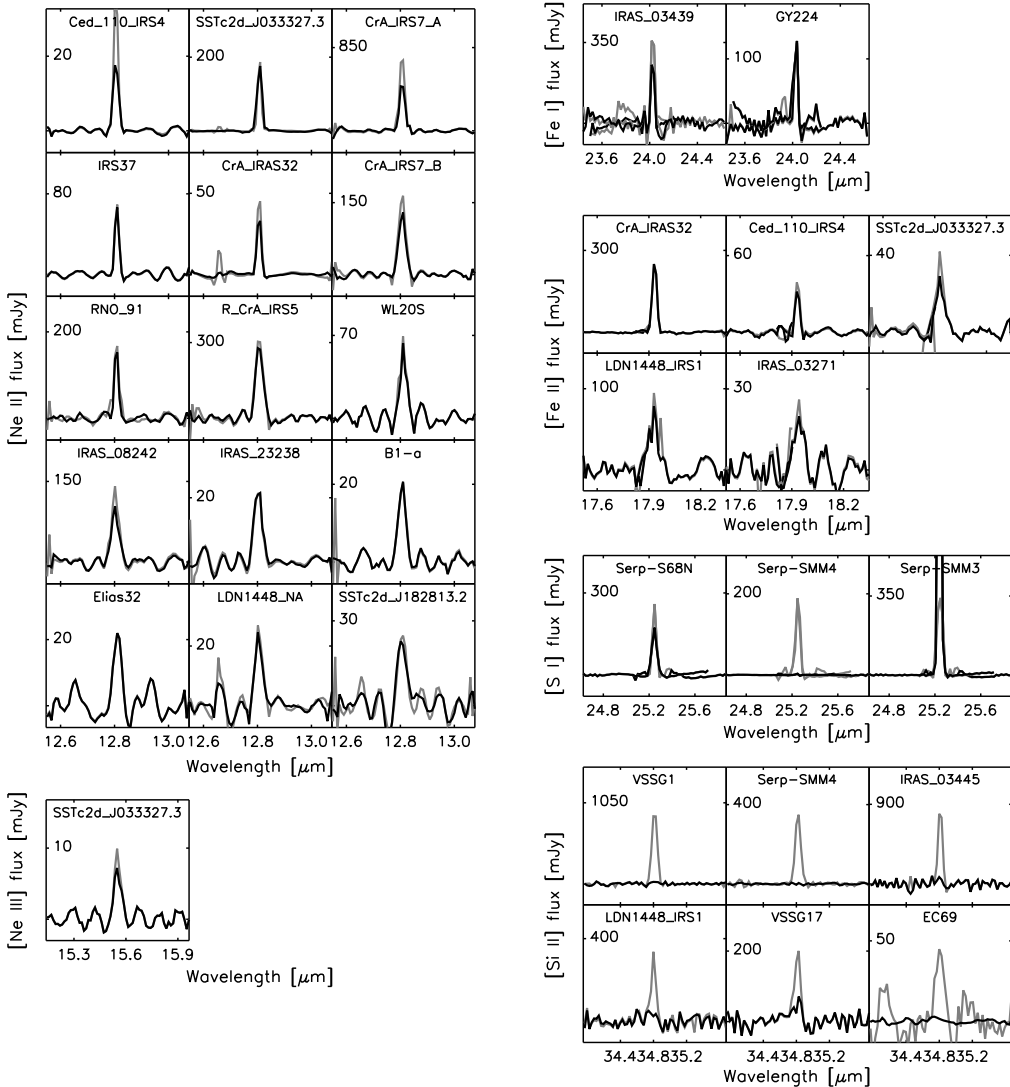


Figure 6.2 Detections of [Ne II], [Ne III], [Fe I], [Fe II] $18\mu\text{m}$, [S I] and [Si II] at the $\geq 4\sigma$ level toward the c2d sample of embedded T Tauri stars and T Tauri stars with edge-on disks. Plotted in gray is the total observed emission (compact source + extended component) and in black the emission after correction of the estimated sky component.

A major concern in the analysis of observations toward these young stars is the confusion of compact source and extended emission. The c2d team has developed an optimal extraction (see §3.2.2.2) which allows the separation of both components in the IRS apertures. §5.3 describes the data reduction of both the observations presented in Chapter 5 and this chapter. §5.2.2 describes the mini-maps used to confirm the presence of extended emission and to verify the extended emission components observed with the optimal extraction. Figure 6.1 gives an example of one of the observed minimaps toward VSSG1, one of the embedded sources presented in this chapter.

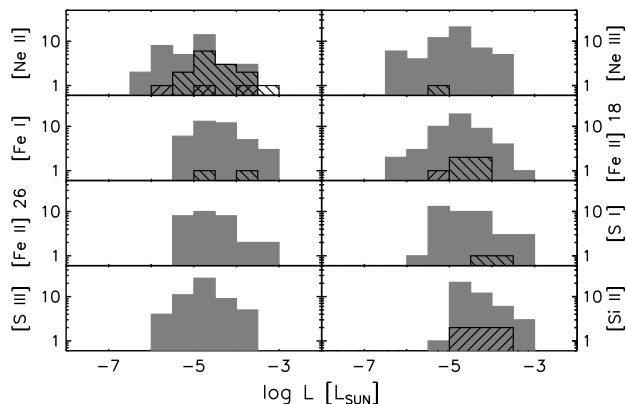


Figure 6.3 Observed line strengths in solar luminosities (hatched bars) and upper limits (solid gray bars) of the major atomic lines. The gray bars include sources without a line detection. The hatched left angled bars are detections of unresolved source emission while the right angled hatched bars are detections of extended line emission.

6.3 Results

6.3.1 Atomic fine-structure lines

Figure 6.2 presents the observed atomic fine-structure lines toward the 56 sources in our sample, while Figure 6.3 shows the distribution of the observed line fluxes and upper limits of the major lines. The gray bars reflect the 4σ upper limits, while the hatched bars represent the detections. Line fluxes for the unresolved and extended components and line flux upper limits are listed in Table 6.2.

Emission lines of [Ne II], [Ne III], [Fe I], [Fe II] $18\mu\text{m}$ (the [Fe II] $26\mu\text{m}$ line is not detected), [S I], and [Si II] are observed toward $\sim 35\%$ of the sources. Of these $\sim 25\%$ show emission from more than one line. The [Ne II], [Ne III], [Fe I], and [Fe II] emission are predominantly unresolved spatially. The [Si II] emission, observed toward $\sim 10\%$ of the sources, is on the other hand always extended. No 4σ detections of [Fe II] $26\mu\text{m}$ and [S III] have been made. The upper limits are of the same order as the line fluxes of the detections (see Figure 6.3).

6.3.2 Molecular hydrogen

Figure 6.4 shows the detections of H_2 emission lines toward the 56 sources in our sample. Except for the H_2 S(0) and S(6) lines all lines observable with the *Spitzer* IRS have been observed toward one or more sources. The H_2 line fluxes for the unresolved and extended components and the line flux upper limits are listed in Table 6.3.

The warm gas ($T_{\text{ex}} \sim 100 - 300$ K traced by the lower rotational lines) is mostly extended. The highest rotational lines ($J = 5$ and 7) are observed toward two sources, IRAS 03271+3013 and SSTc2d J033327.3+310710 and trace hot ($T_{\text{ex}} \sim 1000 - 1500$ K) gas. For $J \geq 5$ no estimate of extended emission is available because the IRS is undersampled at these wavelength and the optimal extraction does not work. Since the $J = 2, 3$, and 4 lines of both sources are mostly unresolved, the observed $J = 5$ and 7 lines are assumed to be unresolved as well in our further analysis.

Care should be taken with the $J = 4$ lines. This line is located near the edge of SL order 1 and is most sensitive to artifacts. Some of the lines presented in Figure 6.4 may therefore be suspect.

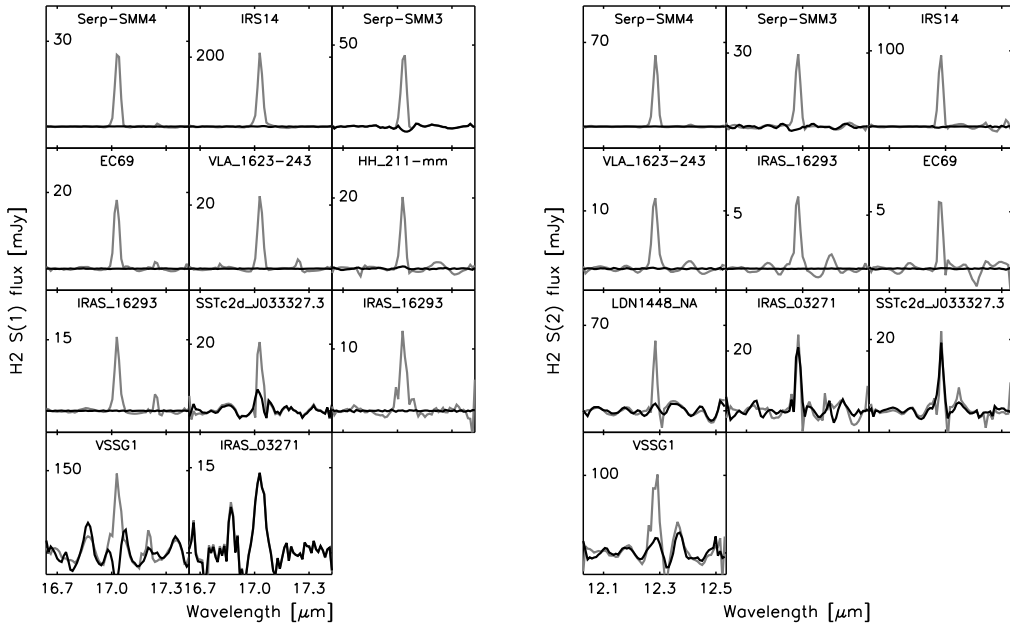


Figure 6.4 Detections of H_2 emission lines at the $\geq 5\sigma$ level toward the c2d sample of embedded T Tauri stars or T Tauri stars with edge-on disks. Plotted in gray is the total observed emission (compact source + extended component) and in black the emission after correction of the estimated sky component. For H_2 S(5) and S(7) no extended emission estimates are available.

In the simplest analysis, the H_2 excitation is assumed to be in local thermal equilibrium (LTE) (e.g., Thi et al., 2001) with an ortho-to-para ratio determined by the kinetic temperature of the gas (following Sternberg & Neufeld, 1999). For gas temperatures 100, 150, and ≥ 200 K, the ortho-to-para ratios are 1.6, 2.5, and 3, respectively. Assuming optically thin emission, the integrated flux of a rotational line $J_u \rightarrow J_l$ for a given temperature T_{ex} is

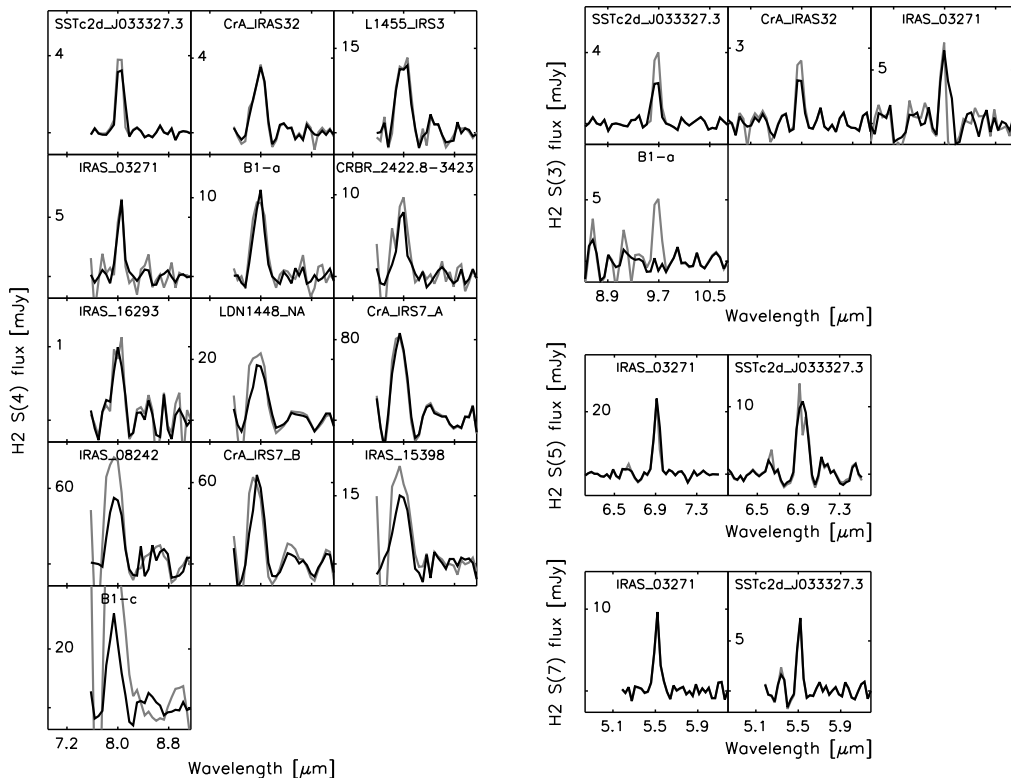
$$F_{ul}(T_{\text{ex}}) = \frac{hc}{4\pi\lambda} N(\text{H}_2) A_{ul} x_u(T_{\text{ex}}) \Omega \text{ erg s}^{-1} \text{ cm}^{-2}, \quad (6.1)$$

where λ is the wavelength of the transition, $N(\text{H}_2)$ the total column density, A_{ul} the spontaneous transition probability, and Ω the source size. For high enough densities ($n \gtrsim 10^3 \text{ cm}^{-3}$), the population x_u follows the Boltzmann law

$$x_u(T_{\text{ex}}) = \frac{g_N(2J_u + 1)e^{-E_J/kT_{\text{ex}}}}{Q(T_{\text{ex}})} \quad (6.2)$$

where E_J is the energy of the upper level, g_N is the nuclear statistical weight (1 for para and 3 for ortho H_2), and $Q(T_{\text{ex}})$ the partition function for the given excitation temperature T_{ex} .

Using the above equations, excitation temperatures, column densities and H_2 gas masses, or limits on these, can be derived from the observed line fluxes and upper limits. If either S(0) or S(1) are detected, an upper or lower limit on the temperature of



– Figure 6.4 continued –

the warm gas is derived, but if neither are detected a temperature of 100 K is assumed for the warm gas. If two or more higher excitation lines (S(2) and higher) are detected an additional temperature for the hot component is derived; otherwise a temperature of 1000 K is assumed for this component. This is done for both spatial components. For five sources a temperature for the extended component can be derived (see §6.4.1.2 and Figure 6.8) and for three sources a temperature of the hot component spatially unresolved component can be derived (see §6.4.3 and Figure 6.10).

The column density averaged over the IRS aperture is derived from the above equations, given the distance to the source. For all unresolved source emission the emitting source size is smaller than the IRS aperture (Sec. 5.3) and since this is unknown a typical size $r = 50$ AU is assumed (see Section 6.4.3) for the emitting region (the derived column density scales as $1/r^2$). The fitted or assumed excitation temperature plus the (upper level) column densities give a total column density or upper limit thereof, which in turn gives the total H_2 gas mass in Jovian masses, $M = \pi r^2 \times N \times 2m_H/M_J$ with $m_H = 1.674 \cdot 10^{-24}$ gr and $M_J = 1.9 \cdot 10^{30}$ gr. Note that the derived gas mass is independent of the assumed beam or source size. The derived H_2 parameters of the unresolved source component for both the warm and hot gas are listed in Table 6.4.

Figure 6.6 shows the distribution of the derived H_2 masses for assumed excitation temperatures of 100 K and 1000 K. The gray bars are upper limits on the gas mass. The hatched bars include sources with H_2 detected. Sources with the S(1) line detected are

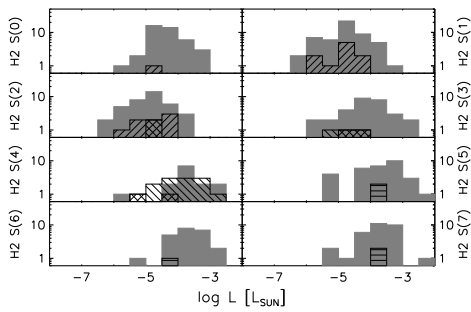


Figure 6.5 Observed H_2 line strengths in solar luminosities (hatched bars) and upper limits (solid gray bars). The gray bars include sources without a line detection. The hatched left angled bars are detections of unresolved source emission while the right angled hatched bars are detections of extended line emission. The horizontal hatched bars indicate that for these lines the optimal extraction does not work and hence no unresolved or extended classification can be assigned.

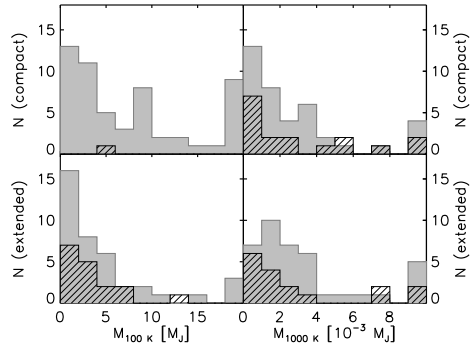


Figure 6.6 Distribution of H_2 masses for both the compact and the extended component assuming $T_{\text{ex}} = 100$ and 1000 K. The gray bars represent upper limits on the gas mass, while the hatched bars indicate sources where H_2 is detected at 4σ or more. For 100 K this includes sources with the H_2 S(1) line detected and for 1000 K sources with any of the higher J lines detected. The highest bar also includes all sources with masses higher than the upper plot limit.

included in the 100 K distribution and sources with any of the higher J lines detected are included in the 1000 K distribution.

6.3.3 Correlations

Figure 6.7 shows the observed line strengths as functions of the apparent optical depth of the $9.8\mu\text{m}$ SiO band estimated from the *Spitzer* IRS spectra. The panels on the left show the observed extended emission. Both the detected [Si II] and the H_2 S(1) and S(2) lines are concentrated toward sources with a low optical depth, $\tau_{9.8} \lesssim 1$ (see §6.4.1.2). The detected H_2 S(4), [Ne II] and [Fe II] $18\mu\text{m}$ lines are more evenly spread with $\tau_{9.8}$. No similar line strength correlation or separation in the distribution is found for other parameters such as the mid-IR luminosity or the mid-IR spectral slope.

6.4 Discussion

Atomic fine structure lines and H_2 pure rotational emission lines are detected toward approximately half of the sources. Both unresolved and extended emission is observed. The unresolved emission is dominated by [Ne II], [Fe II] $18\mu\text{m}$, and high- J H_2 emission lines, while the extended emission is dominated by emission of [Si II] and H_2 S(1) and S(2) emission lines. In the following sections we will compare the observations with shock and PDR models.

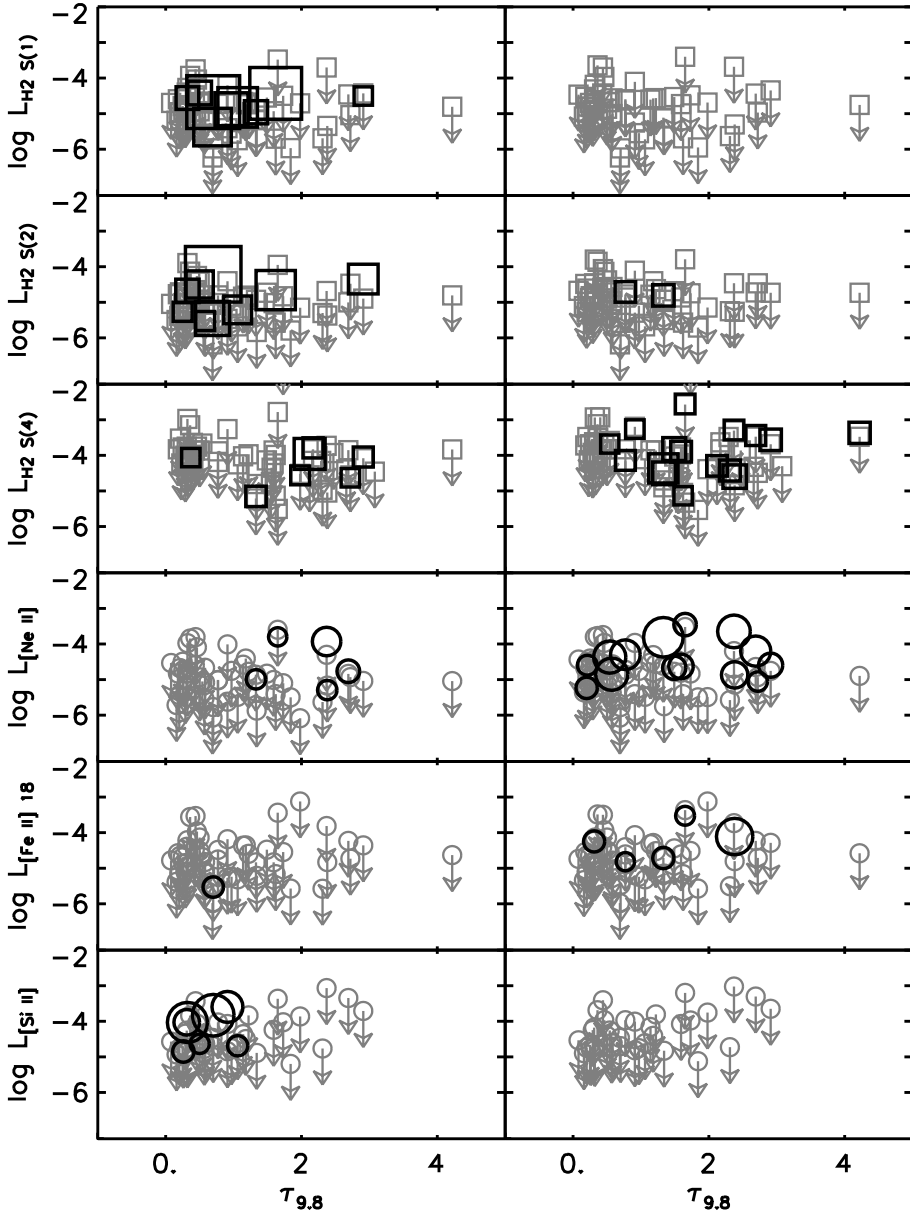


Figure 6.7 Observed line strengths and upper limits (in solar luminosities) as functions of the apparent silicate optical depth estimated from the IRS spectra. The left panel displays the extended emission component, the right the spatially unresolved component. Plotted with the black symbols are the line detections (at 4σ for H_2 and 3σ for the atomic lines), while plotted with small gray symbols and arrows are the upper limits for all non-detections. The size of the black symbols is proportional to the line $\text{SNR}^{1/3}$.

6.4.1 Extended emission

[Si II] and H₂ S(1) and S(2) are the strongest emission lines detected in the spatially extended emission. The observed line fluxes range from $\sim (0.1 - 2) \times 10^{-13}$ erg cm⁻² s⁻¹ for [Si II] and $\sim (0.01 - 1) \times 10^{-13}$ erg cm⁻² s⁻¹ for H₂. For the fully extended emission from IRS this corresponds to $\sim 2 \times 10^{-6} - 4 \times 10^{-5}$ erg cm⁻² s⁻¹ sr⁻¹ for [Si II] and $\sim 10^{-6} - 10^{-4}$ erg cm⁻² s⁻¹ sr⁻¹ for H₂ given the IRS apertures of ~ 230 and 60 arcsec², assuming filling factors of unity.

For a number of sources both the H₂ S(1) and S(2) lines are observed. Figure 6.8 shows the excitation diagrams for five embedded sources. The excitation temperatures derived from both lines, assuming a single component, range from $\sim 350 - 700$ K.

6.4.1.1 Shock excitation

[Si II] is predicted to be one of the strongest mid-IR lines for low velocity $\lesssim 40$ km s⁻¹ shocks (Hollenbach & McKee, 1989). For moderate density gas ($n \sim 10^3$ cm⁻³) the predicted line intensity is comparable to the observed line strengths. However the predicted H₂ $J = 0, 1$ and 2 line strengths are orders of magnitude lower. Higher H₂ line strengths are predicted for higher densities. However, for higher densities other fine structure lines such as [S I] and [Fe II] become stronger and would have been detected given the current sensitivity. A shock origin of the spatially extended [Si II] and H₂ emission is therefore unlikely.

6.4.1.2 PDR excitation

Models of photodissociation regions (PDRs) predict line strengths for [Si II] and H₂ S(1) and S(2) comparable to the observed line strengths for $n \sim 10^2 - 10^5$ cm⁻³ and a radiation field of $\sim 10^1 - 10^3 G_0$ (Hollenbach et al., 1991; Kaufman et al., 2006). The predicted line strengths for [Fe II] and H₂ S(0) are $\sim 5 - 10$ times weaker, consistent with their non-detection in our sample. The H₂ excitation temperatures of $\sim 350 - 700$ K (see Figure 6.8) are consistent with gas surface temperatures for PDRs with the range of densities and radiation fields mentioned above (Kaufman et al., 1999, and the PDRT¹).

The extended [Si II] and H₂ S(1) and S(2) emission is observed more toward sources with low extinction ($\tau_{9.8} \lesssim 1$ or $A_v \lesssim 18$). Two PDR heating scenarios are possible. The first is that the PDRs in the extended envelope are heated by the internal sources and can therefore only be seen for sources with a thin envelope. The second possibility is that the PDRs are on the outer surface of the envelope heated by the external radiation field. The fact that the PDRs are preferentially seen toward low extinction sources could then imply that the environment, among others a strong radiation field, is determining the envelope characteristics of the embedded sources.

6.4.2 Spatially unresolved emission

Spatially unresolved emission is observed in [Ne II], [Fe I], [Fe II], [S I], and H₂. Most unresolved H₂ emission is seen in the H₂ S(4) line suggesting the presence of hot ($T_{\text{ex}} \gtrsim 500$ K) gas. For two embedded sources, IRAS 03271+3013 and SSTc2d J033327.3+310710,

¹Photo Dissociation Region Toolbox <http://dustem.astro.umd.edu/pdrt/>

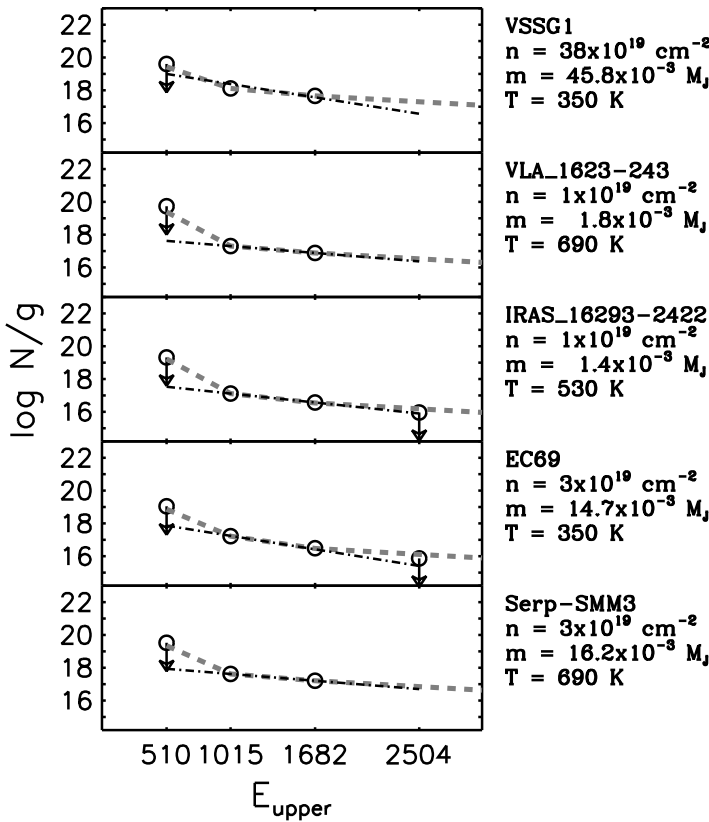


Figure 6.8 Excitation diagrams for five of the sources with multiple extended H₂ emission. The black dash-dot line shows a single temperature fit to the detected S(1) and S(2) emission. The upper limits on S(0) do not exclude the presence of colder ($T_{\text{ex}} \sim 100$ K) gas. The gray dashed line is a fit to both detections and upper limits assuming the two temperatures of 100 K and 1000 K used in Table 6.4.

emission up to the S(7) line is observed. Excitation temperatures of $\sim 1300 - 1500$ K are derived for these sources (see §6.4.3).

The detection of strong atomic lines and hot H₂ suggests the presence of high velocity J -shocks (Hollenbach & McKee, 1989). The observed line fluxes of $\sim 10^{-14} - \text{few} \times 10^{-13}$ for a source unresolved for IRS corresponds to line strengths in the range of $\sim 10^{-4} - 10^{-3} \text{ erg cm}^{-2} \text{ s}^{-1} \text{ sr}^{-1}$ or more. This is consistent with the typical line strength predicted for high velocity ($v_s \gtrsim 50 \text{ km s}^{-1}$) shocks for $n \gtrsim 10^5 \text{ cm}^{-3}$.

Figure 6.9 shows the line ratios of [Ne II] with other atomic and H₂ lines plus the ratios derived from the models presented in Hollenbach & McKee (1989). This shows that the observed line flux ratios and the lower limits for most sources are consistent with those predicted by high velocity J -shocks. The limited number of multiple line detections for individual sources prohibits a more quantitative characterization of the observed shock phenomena, however.

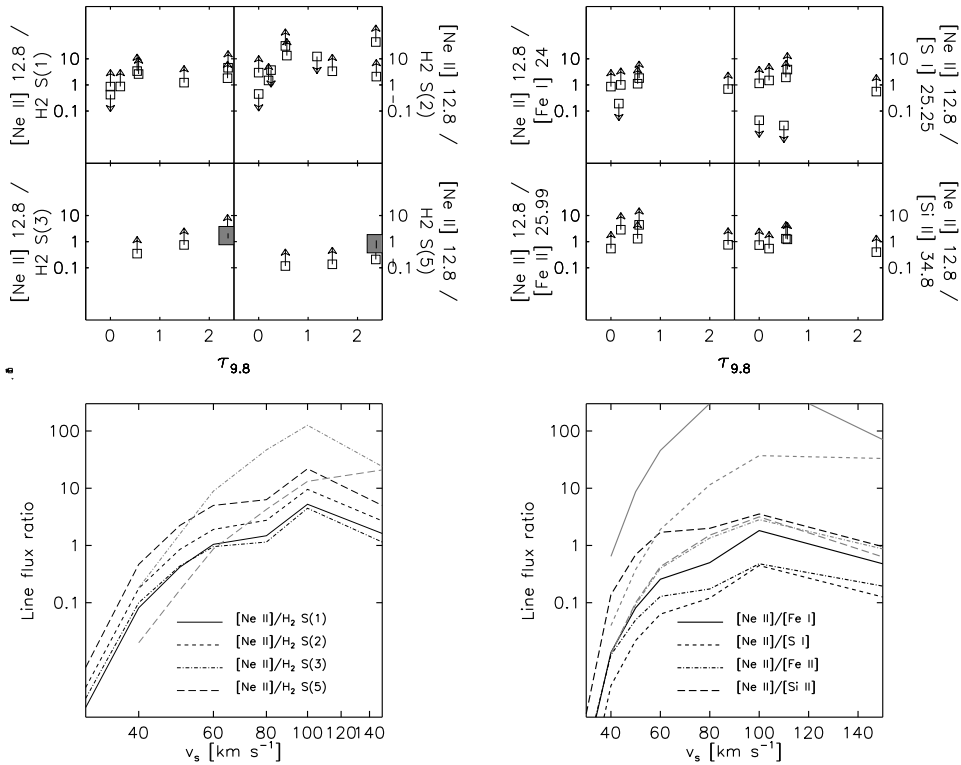


Figure 6.9 [Ne II] line ratios as function of the apparent silicate optical depth. Large filled symbols are used for sources with both [Ne II] and the second line detected. Small open symbols with arrows indicate upper limits or lower limits of the line ratios. The lower two plots show the ratios from shock models by Hollenbach & McKee (1989).

6.4.3 Hot H₂

Toward three sources a temperature of the hot ($T_{\text{ex}} \sim 1300 - 1500$ K) H₂ component can be derived. Figure 6.10 shows the excitation diagrams for these sources. Since the emission is unresolved and no size for the hot gas emitting region is known, a source size has to be assumed to derive a column density. It should be noted that for all three sources the H₂ S(3) ($E_u = 2504$ K) line appears to be weaker than expected given the observed fluxes and upper limits of the other H₂ lines. The S(3) line coincides with the SiO 9.8 μm feature, therefore its reduced line strength shows the emitting region is embedded and located near the central star rather than near the outer surface of the envelope.

For CrA IRAS32 only the S(3) and S(4) lines are observed giving an added uncertainty on the derived excitation temperature. The excitation temperature can however not be higher given the upper limits of the S(5) to S(7) lines. This again illustrates the effect of extinction on the S(3) line. A lower limit of $T_{\text{ex}} \sim 1000$ K is obtained from the upper limits on the S(1) and S(2) lines. This gives an upper limit on the column density and mass of $N \sim 1 \times 10^{20} \text{ cm}^{-2}$ and $M \sim 0.015 M_{\text{J}}$.

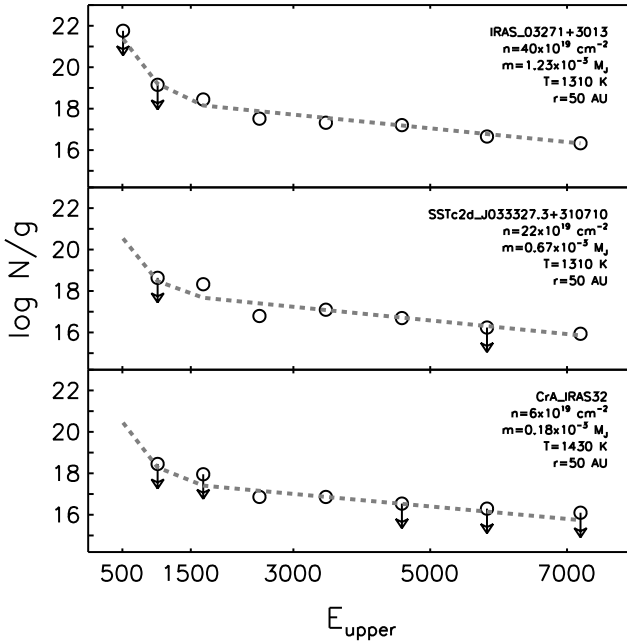


Figure 6.10 Excitation diagrams of the sources revealing hot spatially unresolved H_2 emission. A source size for the emitting region of $r = 50$ AU is assumed to obtain an estimate of the column density. The dashed line shows the fit assuming 100 K for the warm component.

The observed gas masses of a few $10^{-3} M_J$ imply an emission area $r \lesssim 50$ AU assuming a density $n \gtrsim 10^5 \text{ cm}^{-3}$, as suggested by the shock models. It is therefore possible that the observed unresolved emission lines are tracing shocks associated with the base of the outflows close to the embedded star, or shocks due to the accretion onto the disk. The reduced S(3) line strength suggesting a large extinction toward the emitting region is consistent with this. An origin through shocks in the extended envelope as a result of the outflow seems less likely given the small surface area of the emission and the extinction observed through the S(3) line.

6.5 Conclusions

A survey of the mid-infrared gas phase pure rotational lines of molecular hydrogen and a number of atomic fine structure transitions has been carried out toward a sample of 56 embedded protostars and edge-on circumstellar disks with the *Spitzer* IRS. Both spatially resolved and unresolved emission has been detected toward multiple sources. The principal findings include:

- [Ne II], [Fe I], [Fe II], and [Si I] emission is observed predominantly as compact emission toward $\sim 35\%$ of the sources. In contrast, [Si II] is only observed from the extended component.
- The lower pure rotational H_2 emission lines, S(1) and S(2) are detected mostly as extended emission while S(3) and S(4) emission is mostly unresolved.
- The extended [Si II] and warm H_2 emission ($T_{\text{ex}} \lesssim 700$ K) likely originates in a photodissociation region, or PDR, associated with the extended envelope.

- The PDRs are concentrated toward sources with a low apparent optical depth of the $9.8\mu\text{m}$ silicate band ($\tau_{9.8} \lesssim 1$ or $A_v \lesssim 18$). This suggests the PDRs exist in a thin envelope heated by the central star or the PDRs are heated by the external radiation field which influences the envelope characteristics.
- The spatially unresolved atomic fine structure and H_2 lines are consistent with an origin in high velocity J -shocks.
- The observed masses of the hot shocked gas set a size limit to the emitting regions of $r \lesssim 50$ AU suggesting suggesting that the shocks are associated with the outflow base close to the star, or shocks due to the accretion onto the disk.
- Intuitively, spatially unresolved PDR emission from the inner envelope and extended shock emission from the outflow impacting on the envelope would be expected. This is not observed. On the contrary, we observe extended PDR emission and unresolved shock emission.

The sources revealing atomic fine structure line emission and H_2 emission are excellent candidates for follow up with future near-IR and far-IR instruments. Higher spectral and spatial resolution constraints on the mid-IR line emission plus the major cooling lines of [OI] and [CII] in the far-IR, will be important to test the proposed excitation mechanisms of the observed emission. Spectrally resolved line profiles can further distinguish shocks from PDRs whereas high spatial resolution subarcsec data can confirm our conclusions on compact versus extended emission.

Acknowledgements

Astrochemistry in Leiden is supported by a NWO Spinoza grant and a NOVA grant. Support for this work, part of the Spitzer Legacy Science Program, was provided by NASA through contract 1224608 issued by the Jet Propulsion Laboratory, California Institute of Technology, under NASA contracts 1407, 1256316, and 1230779. We thank the Lorentz Center in Leiden for hosting several meetings that contributed to this paper.

Table 6.1. Source list

#	Source	RA	Dec	AOR	tint [s] (SL/SH/LH)/ndiith.	D ^a [pc]
1	LDN1448 IRS1	3 ^h 25 ^m 09 ^s .4	30° 46' 21".7	5656832	(14*1/31*2/60*1)*2	250
2	LDN1448 NA	3 ^h 25 ^m 36 ^s .5	30° 45' 21".2	5828096	(60*1/121*2/60*1)*2	250
3	IRAS 03245+3002	3 ^h 27 ^m 39 ^s .0	30° 12' 59".4	6368000	(14*4/31*4/60*1)*2	250
4	L1455 SMM1	3 ^h 27 ^m 43 ^s .2	30° 12' 28".8	15917056	(60*2/121*2/-)*2	250
5	L1455 IRS3	3 ^h 28 ^m 00 ^s .4	30° 08' 01".3	15917568	(14*4/121*2/-)*2	250
6	IRAS 03254+3050	3 ^h 28 ^m 34 ^s .5	31° 00' 51".1	11827200	(14*2/31*2/60*1)*2	250
7	IRAS 03271+3013	3 ^h 30 ^m 15 ^s .2	30° 23' 48".8	5634304	(14*2/31*4/60*1)*2	250
8	IRAS 03301+3111	3 ^h 33 ^m 12 ^s .8	31° 21' 24".1	5634560	(14*1/6*2/14*2)*2	250
9	B1-a	3 ^h 33 ^m 16 ^s .7	31° 07' 55".2	15918080	(14*4/31*2/-)*2	250
10	B1-c	3 ^h 33 ^m 17 ^s .9	31° 09' 31".0	13460480	(14*2/31*2/-)*2	250
11	SSTc2d J033327.3+310710	3 ^h 33 ^m 27 ^s .3	31° 07' 10".2	15918336	(60*3/121*2/-)*2	250
12	HH 211-mm	3 ^h 43 ^m 56 ^s .8	32° 00' 50".4	5826304	(-/31*2/60*2)*2	250
13	IRAS 03439+3233	3 ^h 47 ^m 05 ^s .4	32° 43' 08".4	5635072	(14*1/121*2/60*1)*2	250
14	IRAS 03445+3242	3 ^h 47 ^m 41 ^s .6	32° 51' 43".9	5635328	(14*1/6*2/14*1)*2	250
15	IRAS 08242-5050	8 ^h 25 ^m 43 ^s .8	-51° 00' 35".6	5638912	(14*1/6*2/14*1)*2	460
16	IRAS 08261-5100	8 ^h 27 ^m 38 ^s .9	-51° 10' 37".2	5638912	(14*1/6*2/14*1)*2	400
17 ^b	Ced 110 IRS4	11 ^h 06 ^m 46 ^s .6	-77° 22' 32".5	5639680	(-/121*2/60*2)*2	178
18	IRAS 12553-7651	12 ^h 59 ^m 06 ^s .6	-77° 07' 40".1	9830912	(14*1/31*1/60*1)*2	178
19	IRAS 13546-3941	13 ^h 57 ^m 38 ^s .9	-39° 56' 00".2	5642752	(14*1/31*2/60*1)*2	630
20	IRAS 15398-3359	15 ^h 43 ^m 02 ^s .3	-34° 09' 06".8	5828864	(14*2/31*6/60*1)*2	100
21	VSSG1	16 ^h 26 ^m 18 ^s .9	-24° 28' 19".6	5647616	(-/31*1/14*2)*2	125
22 ^b	GSS30-IRS1	16 ^h 26 ^m 21 ^s .4	-24° 23' 04".2	5647616	(-/31*1/14*2)*2	125
23	GY23	16 ^h 26 ^m 24 ^s .1	-24° 24' 48".2	5647616	(-/31*1/14*2)*2	125
24	VLA 1623-243	16 ^h 26 ^m 26 ^s .4	-24° 24' 30".2	9828096	(-/121*4/60*4)*2	125
25	IRS14	16 ^h 26 ^m 31 ^s .0	-24° 31' 05".2	12664576	(60*2/31*1/-)*2	125
26	WL12	16 ^h 26 ^m 44 ^s .2	-24° 34' 48".4	5647616	(-/31*1/14*2)*2	125
27	OphE-MM3	16 ^h 27 ^m 05 ^s .9	-24° 37' 08".0	6370816	(60*5/31*8/60*2)*2	125
28	GY224	16 ^h 27 ^m 11 ^s .2	-24° 40' 46".6	9829888	(-/31*2/14*2)*2	125
29	WL19	16 ^h 27 ^m 11 ^s .7	-24° 38' 32".3	9829888	(-/31*2/14*2)*2	125
30	WL20S	16 ^h 27 ^m 15 ^s .6	-24° 38' 45".6	9829888	(-/31*2/14*2)*2	125
31	IRS37	16 ^h 27 ^m 17 ^s .6	-24° 28' 56".6	5647616	(-/31*1/14*2)*2	125
32	WL6	16 ^h 27 ^m 21 ^s .8	-24° 29' 53".2	5647616	(-/31*1/14*2)*2	125
33 ^b	CRBR 2422.8-3423	16 ^h 27 ^m 24 ^s .6	-24° 41' 03".1	9346048	(14*1/121*1/241*2)*2	125
34	Elias32	16 ^h 27 ^m 28 ^s .4	-24° 27' 21".2	12664320	(-/31*2/60*2)*2	125
35 ^b	IRS46	16 ^h 27 ^m 29 ^s .4	-24° 39' 16".2	9829888	(-/31*2/14*2)*2	125
36	VSSG17	16 ^h 27 ^m 30 ^s .2	-24° 27' 43".6	5647616	(-/31*1/14*2)*2	125
37	IRS63	16 ^h 31 ^m 35 ^s .7	-24° 01' 29".6	9827840	(-/31*1/14*1)*2	125
38	L1689-IRS5	16 ^h 31 ^m 52 ^s .1	-24° 56' 15".4	12664064	(-/31*1/60*1)*2	125
39	IRAS 16293-2422B	16 ^h 32 ^m 22 ^s .6	-24° 28' 32".2	15735808	(60*1/121*4/60*4)*2	125
40	IRAS 16293-2422	16 ^h 32 ^m 22 ^s .9	-24° 28' 36".1	11826944	(60*1/121*4/60*4)*2	125
41 ^b	RNO 91	16 ^h 34 ^m 29 ^s .3	-15° 47' 01".3	5650432	(14*1/31*1/14*2)*2	140
42	SSTc2d J182813.2+00313	18 ^h 28 ^m 13 ^s .2	0° 03' 13".0	13210368	(14*1/31*2/-)*2	260
43	SSTc2d J182849.4+00604	18 ^h 28 ^m 49 ^s .4	-0° 06' 04".7	13210624	(14*1/31*1/-)*2	260
44	SSTc2d J182901.8+02954	18 ^h 29 ^m 01 ^s .8	0° 29' 54".2	13210112	(14*1/31*2/-)*2	260
45	SSTc2d J182914.8+00424	18 ^h 29 ^m 14 ^s .8	-0° 04' 23".9	13210112	(14*1/31*2/-)*2	260
46	SSTc2d J182916.2+01822	18 ^h 29 ^m 16 ^s .2	0° 18' 22".7	13210112	(14*1/31*2/-)*2	260
47	Serp-S68N	18 ^h 29 ^m 48 ^s .1	1° 16' 42".6	9828608	(-/121*4/60*4)*2	260
48	EC69	18 ^h 29 ^m 54 ^s .4	1° 15' 01".8	9407232	(14*1/121*1/60*2)*2	260
49	Serp-SMM4	18 ^h 29 ^m 56 ^s .6	1° 13' 15".2	9828608	(-/121*4/60*4)*2	260
50	EC88	18 ^h 29 ^m 57 ^s .6	1° 13' 00".5	9407232	(14*1/121*1/60*2)*2	260
51	Serp-SMM3	18 ^h 29 ^m 59 ^s .2	1° 14' 00".2	9828608	(-/121*4/60*4)*2	260
52	R CrA IRS5	19 ^h 01 ^m 48 ^s .0	-36° 57' 21".6	9835264	(14*1/6*2/-)*2	130
53	CrA IRS7 A	19 ^h 01 ^m 55 ^s .3	-36° 57' 22".0	9835008	(14*1/31*3/60*2)*2	170
54	CrA IRS7 B	19 ^h 01 ^m 56 ^s .4	-36° 57' 28".1	9835008	(14*1/31*3/60*2)*2	170
55	CrA IRS32	19 ^h 02 ^m 58 ^s .7	-37° 07' 34".7	9832192	(60*1/31*8/-)*2	170
56	IRAS 23238+7401	23 ^h 25 ^m 46 ^s .7	74° 17' 37".3	9833728	(14*1/31*8/60*2)*2	250

^aSee footnote *a* of Table 5.1.^bKnown or candidate edge-on-disks

Table 6.2. Observed linefluxes and 1σ uncertainties ($10^{-16}\text{erg cm}^{-2}\text{s}^{-1}$)

#	Source	[Ne II]			[Ne III]			[Fe I] 24.04		
		src	ext	upp	src	ext	upp	src	ext	upp
1	LDN1448 IRS1	-	-	(36)	-	-	(57)	-	-	(68)
2	LDN1448 NA	130	-	(18)	-	-	(23)	-	-	(100)
3	IRAS 03245+3002	-	-	(3)	-	-	(13)	-	-	(56)
4	L1455 SMM1	-	-	(12)	-	-	(5)	-	-	-
5	L1455 IRS3	-	-	(15)	-	-	(8)	-	-	-
6	IRAS 03254+3050	-	-	(28)	-	-	(29)	-	-	(140)
7	IRAS 03271+3013	-	-	(14)	-	-	(13)	-	-	(89)
8	IRAS 03301+3111	-	-	(110)	-	-	(92)	-	-	(140)
9	B1-a	110	-	(17)	-	-	(19)	-	-	-
10	B1-c	-	-	(13)	-	-	(7)	-	-	-
11	SSTc2d J033327.3	790	-	(25)	34	-	(6)	-	-	-
12	HH 211-mm	-	-	(18)	-	-	(3)	-	-	(39)
13	IRAS 03439+3233	-	-	(7)	-	-	(17)	700	-	(99)
14	IRAS 03445+3242	-	-	(110)	-	-	(59)	-	-	(100)
15	IRAS 08242-5050	530	-	(91)	-	-	(77)	-	-	(140)
16	IRAS 08261-5100	-	-	(67)	-	-	(69)	-	-	(67)
17	Ced 110 IRS4	74	13	(4)	-	-	(9)	-	-	(65)
18	IRAS 12553-7651	-	-	(61)	-	-	(50)	-	-	(150)
19	IRAS 13546-3941	-	-	(18)	-	-	(21)	-	-	(44)
20	IRAS 15398-3359	-	-	(17)	-	-	(13)	-	-	(55)
21	VSSG1	-	-	(55)	-	-	(54)	-	-	(55)
22	GSS30-IRS1	-	-	(730)	-	-	(1000)	-	-	(2000)
23	GY23	-	-	(160)	-	-	(82)	-	-	(68)
24	VLA 1623-243	-	-	(3)	-	-	(1)	-	-	(77)
25	IRS14	-	-	(16)	-	-	(4)	-	-	-
26	WL12	-	-	(200)	-	-	(180)	-	-	(180)
27	OphE-MM3	-	-	(13)	-	-	(3)	-	-	(31)
28	GY224	-	-	(18)	-	-	(24)	280	-	(38)
29	WL19	-	-	(16)	-	-	(16)	-	-	(42)
30	WL20S	310	-	(34)	-	-	(59)	-	-	(120)
31	IRS37	290	-	(17)	-	-	(23)	-	-	(53)
32	WL6	-	-	(110)	-	-	(77)	-	-	(140)
33	CRBR 2422.8-3423	-	-	(7)	-	-	(17)	-	-	(66)
34	Elias32	120	-	(24)	-	-	(26)	-	-	(40)
35	IRS46	-	-	(38)	-	-	(32)	-	-	(59)
36	VSSG17	-	-	(99)	-	-	(63)	-	-	(59)
37	IRS63	-	-	(72)	-	-	(64)	-	-	(94)
38	L1689-IRS5	-	-	(150)	-	-	(97)	-	-	(130)
39	IRAS 16293-2422B	-	-	(16)	-	-	(5)	-	-	(48)
40	IRAS 16293-2422	-	-	(2)	-	-	(2)	-	-	(33)
41	RNO 91	700	-	(41)	-	-	(95)	-	-	(210)
42	SSTc2d J182813.2	-	-	(30)	-	-	(24)	-	-	-
43	SSTc2d J182849.4	-	-	(150)	-	-	(49)	-	-	-
44	SSTc2d J182901.8	-	-	(20)	-	-	(23)	-	-	-
45	SSTc2d J182914.8	-	-	(17)	-	-	(18)	-	-	-
46	SSTc2d J182916.2	-	-	(27)	-	-	(35)	-	-	-
47	Serp-S68N	-	-	(6)	-	-	(6)	-	-	(38)
48	EC69	-	-	(3)	-	-	(1)	-	-	(11)
49	Serp-SMM4	-	-	(1)	-	-	(2)	-	-	(26)
50	EC88	-	-	(14)	-	-	(24)	-	-	(72)
51	Serp-SMM3	-	-	(6)	-	-	(5)	-	-	(42)
52	R CrA IRS5	1600	-	(120)	-	-	(180)	-	-	-
53	CrA IRS7 A	2500	1300	(140)	-	-	(480)	-	-	(1200)
54	CrA IRS7 B	700	190	(50)	-	-	(130)	-	-	(680)
55	CrA IRAS32	150	-	(16)	-	-	(10)	-	-	-
56	IRAS 23238+7401	120	-	(16)	-	-	(14)	-	-	(56)

Table 6.2. – continued –

	[Fe II] 17.94			[Fe II] 25.99			[S I]			[Si II]		
	src	ext	upp	src	ext	upp	src	ext	upp	src	ext	upp
1	290	–	(60)	–	–	(67)	–	–	(51)	–	480	(68)
2	–	–	(53)	–	–	(100)	–	–	(76)	–	–	(230)
3	–	–	(770)	–	–	(85)	–	–	(120)	–	–	(180)
4	–	–	(20)									
5	–	–	(27)									
6	–	–	(31)	–	–	(67)	–	–	(94)	–	–	(160)
7	–	–	(25)	–	–	(36)	–	–	(55)	–	–	(110)
8	–	–	(120)	–	–	(110)	–	–	(82)	–	–	(110)
9	–	–	(37)									
10	–	–	(27)									
11	99	–	(20)									
12	–	–	(5)	–	–	(9)	–	–	(12)	–	–	(18)
13	–	–	(12)	–	–	(39)	–	–	(39)	–	–	(58)
14	–	–	(87)	–	–	(99)	–	–	(69)	–	1300	(100)
15	–	–	(130)	–	–	(180)	–	–	(150)	–	–	(190)
16	–	–	(130)	–	–	(64)	–	–	(110)	–	–	(82)
17	110	68	(15)	–	–	(29)	–	–	(23)	–	–	(45)
18	–	–	(96)	–	–	(44)	–	–	(130)	–	–	(140)
19	–	–	(43)	–	–	(37)	–	–	(43)	–	–	(43)
20	–	–	(20)	–	–	(49)	–	–	(37)	–	–	(120)
21	–	–	(52)	–	–	(33)	–	–	(50)	–	1900	(64)
22	–	–	(1300)	–	–	(1400)	–	–	(1800)	–	–	(1600)
23	–	–	(92)	–	–	(65)	–	–	(60)	–	–	(89)
24	–	–	(4)	–	–	(73)	–	–	(53)	–	–	(140)
25	–	–	(28)									
26	–	–	(210)	–	–	(230)	–	–	(130)	–	–	(160)
27	–	–	(11)	–	–	(16)	–	–	(19)	–	–	(31)
28	–	–	(19)	–	–	(23)	–	–	(41)	–	–	(52)
29	–	–	(26)	–	–	(28)	–	–	(24)	–	–	(63)
30	–	–	(120)	–	–	(190)	–	–	(90)	–	–	(140)
31	–	–	(33)	–	–	(22)	–	–	(25)	–	–	(79)
32	–	–	(67)	–	–	(140)	–	–	(64)	–	–	(100)
33	–	–	(29)	–	–	(44)	–	–	(32)	–	–	(61)
34	–	–	(33)	–	–	(14)	–	–	(27)	–	–	(74)
35	–	–	(38)	–	–	(50)	–	–	(48)	–	–	(100)
36	–	–	(58)	–	–	(34)	–	–	(41)	–	290	(68)
37	–	–	(62)	–	–	(64)	–	–	(73)	–	–	(79)
38	–	–	(75)	–	–	(58)	–	–	(70)	–	–	(120)
39	–	–	(14)	–	–	(42)	–	–	(51)	–	–	(220)
40	–	–	(4)	–	–	(38)	–	150	(60)	–	–	(180)
41	–	–	(88)	–	–	(180)	–	–	(120)	–	–	(180)
42	–	–	(22)									
43	–	–	(69)									
44	–	–	(27)									
45	–	–	(30)									
46	–	–	(38)									
47	–	–	(16)	–	–	(16)	460	–	(26)	–	–	(45)
48	–	–	(4)	–	–	(2)	–	–	(3)	–	97	(23)
49	–	–	(3)	–	–	(30)	–	370	(15)	–	700	(19)
50	–	–	(29)	–	–	(42)	–	–	(74)	–	–	(100)
51	–	–	(69)	–	–	(24)	740	–	(39)	–	–	(37)
52	–	–	(250)									
53	–	–	(410)	–	–	(1100)	–	–	(1500)	–	–	(2100)
54	–	–	(130)	–	–	(240)	–	–	(310)	–	–	(1100)
55	860	–	(35)									
56	–	–	(25)	–	–	(36)	–	–	(78)	–	–	(86)

Table 6.3. Observed linefluxes and 1σ uncertainties ($10^{-16}\text{erg cm}^{-2}\text{s}^{-1}$)

#	Source	H2 S(1)			H2 S(2)			H2 S(3)		
		src	ext	upp	src	ext	upp	src	ext	upp
1	LDN1448 IRS1	-	-	(49)	-	-	(35)	-	-	(120)
2	LDN1448 NA	-	-	(46)	-	230	(19)	-	-	(200)
3	IRAS 03245+3002	-	-	(21)	-	-	(7)	-	-	(23)
4	L1455 SMM1	-	-	(11)	-	-	(35)	-	-	(22)
5	L1455 IRS3	-	-	(14)	-	-	(15)	-	-	(42)
6	IRAS 03254+3050	-	-	(28)	-	-	(24)	-	-	(67)
7	IRAS 03271+3013	-	-	(26)	100	-	(17)	260	-	(50)
8	IRAS 03301+3111	-	-	(110)	-	-	(73)	-	-	(180)
9	B1-a	-	-	(30)	-	-	(21)	-	240	(49)
10	B1-c	-	-	(18)	-	-	(19)	-	-	(43)
11	SSTc2d J033327.3	-	56	(7)	80	-	(12)	100	74	(14)
12	HH 211-mm	-	68	(2)	-	-	(8)	-	-	-
13	IRAS 03439+3233	-	-	(13)	-	-	(7)	-	-	(61)
14	IRAS 03445+3242	-	-	(80)	-	-	(79)	-	-	(350)
15	IRAS 08242-5050	-	-	(120)	-	-	(49)	-	-	(930)
16	IRAS 08261-5100	-	-	(91)	-	-	(55)	-	-	(290)
17	Ced 110 IRS4	-	-	(10)	-	-	(8)	-	-	-
18	IRAS 12553-7651	-	-	(50)	-	-	(33)	-	-	(120)
19	IRAS 13546-3941	-	-	(28)	-	-	(23)	-	-	(200)
20	IRAS 15398-3359	-	-	(15)	-	-	(36)	-	-	(97)
21	VSSG1	-	560	(97)	-	430	(70)	-	-	-
22	GSS30-IRS1	-	-	(810)	-	-	(350)	-	-	-
23	GY23	-	-	(82)	-	-	(54)	-	-	-
24	VLA 1623-243	-	86	(2)	-	72	(2)	-	-	-
25	IRS14	-	760	(8)	-	450	(11)	-	-	(23)
26	WL12	-	-	(110)	-	-	(160)	-	-	-
27	OphE-MM3	-	-	(4)	-	-	(8)	-	-	(7)
28	GY224	-	-	(34)	-	-	(32)	-	-	-
29	WL19	-	-	(23)	-	-	(21)	-	-	-
30	WL20S	-	-	(120)	-	-	(24)	-	-	-
31	IRS37	-	-	(37)	-	-	(44)	-	-	-
32	WL6	-	-	(110)	-	-	(110)	-	-	-
33	CRBR 2422.8-3423	-	-	(30)	-	-	(13)	-	-	(66)
34	Elias32	-	-	(46)	-	-	(22)	-	-	-
35	IRS46	-	-	(40)	-	-	(25)	-	-	-
36	VSSG17	-	-	(63)	-	-	(61)	-	-	-
37	IRS63	-	-	(76)	-	-	(46)	-	-	-
38	L1689-IRS5	-	-	(140)	-	-	(86)	-	-	-
39	IRAS 16293-2422B	-	50	(4)	-	-	(6)	-	-	(11)
40	IRAS 16293-2422	-	56	(2)	-	35	(2)	-	-	(17)
41	RNO 91	-	-	(69)	-	-	(62)	-	-	(670)
42	SSTc2d J182813.2	-	-	(15)	-	-	(23)	-	-	(140)
43	SSTc2d J182849.4	-	-	(61)	-	-	(150)	-	-	(400)
44	SSTc2d J182901.8	-	-	(28)	-	-	(31)	-	-	(170)
45	SSTc2d J182914.8	-	-	(13)	-	-	(39)	-	-	(86)
46	SSTc2d J182916.2	-	-	(35)	-	-	(24)	-	-	(110)
47	Serp-S68N	-	-	(19)	-	-	(10)	-	-	-
48	EC69	-	71	(1)	-	29	(2)	-	-	(41)
49	Serp-SMM4	-	100	(1)	-	290	(2)	-	-	-
50	EC88	-	-	(31)	-	-	(17)	-	-	(32000)
51	Serp-SMM3	-	180	(20)	-	150	(12)	-	-	-
52	R CrA IRS5	-	-	(150)	-	-	(87)	-	-	(710)
53	CrA IRS7 A	-	-	(460)	-	-	(76)	-	-	(340)
54	CrA IRS7 B	-	-	(81)	-	-	(42)	-	-	(280)
55	CrA IRAS32	-	-	(11)	-	-	(12)	88	-	(17)
56	IRAS 23238+7401	-	-	(19)	-	-	(14)	-	-	(61)

Table 6.3. – continued –

	H2 S(4)			H2 S(5)			H2 S(6)			H2 S(7)		
	src	ext	upp	src	ext	upp	src	ext	upp	src	ext	upp
1	–	–	(240)	–	–	(160)	–	–	(110)	–	–	(170)
2	1400	460	(210)	–	–	(420)	–	–	(380)	–	–	(380)
3	–	–	(42)	–	–	(43)	–	–	(88)	–	–	(67)
4	–	–	(33)	–	–	(57)	–	–	(78)	–	–	(46)
5	950	–	(150)	–	–	(66)	–	–	(57)	–	–	(93)
6	–	–	(140)	–	–	(170)	–	–	(240)	–	–	(160)
7	370	–	(70)	1100	–	(50)	470	–	(92)	640	–	(44)
8	–	–	(200)	–	–	(250)	–	–	(240)	–	–	(230)
9	770	–	(95)	–	–	(270)	–	–	(140)	–	–	(110)
10	2200	–	(340)	–	–	(570)	–	–	(660)	–	–	(680)
11	220	36	(13)	680	–	(68)	–	–	(30)	540	–	(56)
12												
13	–	–	(120)	–	–	(95)	–	–	(100)	–	–	(79)
14	–	–	(650)	–	–	(760)	–	–	(470)	–	–	(720)
15	4200	–	(810)	–	–	(2500)	–	–	(2000)	–	–	(1800)
16	–	–	(300)	–	–	(330)	–	–	(280)	–	–	(200)
17												
18	–	–	(280)	–	–	(300)	–	–	(560)	–	–	(410)
19	–	–	(300)	–	–	(300)	–	–	(210)	–	–	(150)
20	1200	–	(190)	–	–	(260)	–	–	(250)	–	–	(310)
21												
22												
23												
24												
25	–	–	(36)	–	–	(37)	–	–	(53)	–	–	(46)
26												
27	–	–	(12)	–	–	(38)	–	–	(33)	–	–	(21)
28												
29												
30												
31												
32												
33	640	–	(81)	–	–	(160)	–	–	(170)	–	–	(150)
34												
35												
36												
37												
38												
39	78	–	(11)	–	–	(24)	–	–	(25)	–	–	(27)
40	–	–	(23)	–	–	(30)	–	–	(33)	–	–	(37)
41	–	–	(830)	–	–	(2000)	–	–	(2200)	–	–	(2100)
42	–	–	(310)	–	–	(590)	–	–	(570)	–	–	(260)
43	–	–	(1100)	–	–	(1400)	–	–	(2600)	–	–	(700)
44	–	–	(180)	–	–	(160)	–	–	(180)	–	–	(180)
45	–	–	(140)	–	–	(280)	–	–	(230)	–	–	(280)
46	–	–	(140)	–	–	(310)	–	–	(150)	–	–	(200)
47												
48	–	–	(74)	–	–	(89)	–	–	(110)	–	–	(120)
49												
50	–	–	(51000)	–	–	(470)	–	–	(590)	–	–	(520)
51												
52	–	–	(950)	–	–	(1900)	–	–	(1200)	–	–	(870)
53	5700	–	(1100)	–	–	(4000)	–	–	(850)	–	–	(880)
54	4000	–	(740)	–	–	(1100)	–	–	(1400)	–	–	(1000)
55	280	–	(32)	–	–	(58)	–	–	(74)	–	–	(94)
56	–	–	(170)	–	–	(91)	–	–	(140)	–	–	(97)

Table 6.4. H₂ excitation parameters.

#	Source	Warm H ₂ ^a				Hot H ₂ ^a			
		Compact ^b		Extended		Compact ^b		Extended	
		[10 ²² cm ⁻²]	[M _J]	[10 ²⁰ cm ⁻²]	[M _J]	[10 ²⁰ cm ⁻²]	[10 ⁻³ M _J]	[10 ¹⁸ cm ⁻²]	[10 ⁻³ M _J]
1	LDN1448 IRS1	< 440	< 13.5	< 9	< 4.4	< 8	< 2.6	< 5	< 2.7
2	LDN1448 NA	< 640	< 19.4	9	4.8	8	2.8	15	7.3
3	IRAS 03245+3002	< 520	< 16.4	< 14	< 6.9	< 1	< 0.4	< 1	< 0.7
4	L1455 SMM1	< 96	< 3.0	< 4	< 2.3	1	0.6	< 1	< 0.9
5	L1455 IRS3	< 108	< 3.3	< 1	< 0.9	4	1.5	< 8	< 4.1
6	IRAS 03254+3050	< 276	< 8.6	< 7	< 3.5	< 7	< 2.2	< 2	< 1.4
7	IRAS 03271+3013	< 388	< 12.0	< 11	< 5.2	9	2.9	< 2	< 1.2
8	IRAS 03301+3111	< 880	< 26.9	< 9	< 4.6	< 13	< 4.2	< 16	< 7.8
9	B1-a	< 264	< 8.2	< 14	< 7.5	5	1.6	< 3	< 1.9
10	B1-c	< 68	< 2.1	< 8	< 3.9	13	4.3	< 2	< 1.4
11	SSTc2d J033327.3	< 34	< 1.1	8	3.9	4	1.4	1	0.5
12	HH 211-mm	< 56	< 1.7	3	1.6	< 1	< 0.6	7	3.5
13	IRAS 03439+3233	< 280	< 8.6	< 8	< 4.3	< 4	< 1.3	< 2	< 1.2
14	IRAS 03445+3242	< 600	< 18.4	< 12	< 6.1	29	9.0	< 13	< 6.4
15	IRAS 08242-5050	< 2760	< 86.1	< 20	< 32.3	220	68.3	< 23	< 38.1
16	IRAS 08261-5100	< 1840	< 56.7	< 6	< 7.6	< 38	< 11.8	< 16	< 20.0
17	Ced 110 IRS4	< 80	< 2.5	< 4	< 1.0	< 1	< 0.3	< 1	< 0.5
18	IRAS 12553-7651	< 304	< 9.4	< 14	< 3.7	< 6	< 2.0	< 5	< 1.3
19	IRAS 13546-3941	< 1600	< 49.1	5	15.6	< 68	< 21.5	8	25.2
20	IRAS 15398-3359	< 28	< 0.9	< 2	< 0.2	1	0.5	< 3	< 0.3
21	VSSG1	< 144	< 4.4	12	1.5	< 9	< 3.0	66	7.9
22	GSS30-IRS1	< 2160	< 66.8	< 210	< 25.6	< 24	< 7.4	< 44	< 5.3
23	GY23	< 192	< 5.9	< 17	< 2.1	< 3	< 1.1	< 17	< 2.1
24	VLA 1623-243	< 30	< 0.9	10	1.3	< 0.2	< 0.1	5	0.6
25	IRS14	< 16	< 0.5	99	12.3	0.6	0.2	30	3.7
26	WL12	< 256	< 7.9	< 16	< 2.0	< 11	< 3.4	< 28	< 3.4
27	OphE-MM3	< 12	< 0.4	< 1	< 0.2	< 0.3	< 0.1	< 1	< 0.2
28	GY224	< 108	< 3.4	< 14	< 1.7	< 2	< 0.7	< 3	< 0.4
29	WL19	< 76	< 2.4	< 9	< 1.1	< 1	< 0.4	< 2	< 0.3
30	WL20S	< 268	< 8.4	< 14	< 1.9	< 1	< 0.5	< 13	< 1.6

Table 6.4—Continued

#	Source	Warm H ₂ ^a				Hot H ₂ ^a			
		Compact ^b		Extended		Compact ^b		Extended	
		[10 ²² cm ⁻²]	[M _J]	[10 ²⁰ cm ⁻²]	[M _J]	[10 ²⁰ cm ⁻²]	[10 ⁻³ M _J]	[10 ¹⁸ cm ⁻²]	[10 ⁻³ M _J]
31	IRS37	< 88	< 2.8	< 5	< 0.6	< 3	< 0.9	< 15	< 1.8
32	WL6	< 160	< 4.9	< 11	< 1.3	< 11	< 3.6	< 27	< 3.3
33	CRBR 2422.8-3423	< 84	< 2.6	< 9	< 1.1	1	0.5	< 2	< 0.3
34	Elias32	< 44	< 1.4	< 2	< 0.3	< 3	< 1.1	< 14	< 1.7
35	IRS46	< 116	< 3.6	< 12	< 1.6	< 1	< 0.5	< 8	< 1.0
36	VSSG17	< 132	< 4.1	< 7	< 0.9	< 4	< 1.3	< 20	< 2.5
37	IRS63	< 200	< 6.2	< 18	< 2.1	< 3	< 1.0	< 13	< 1.6
38	L1689-IRS5	< 120	< 3.7	< 4	< 0.5	< 13	< 4.3	< 29	< 3.6
39	IRAS 16293-2422B	< 44	< 1.3	6	0.7	0.3	0.1	2	0.3
40	IRAS 16293-2422	< 31	< 1.0	7	0.9	< 0.3	< 0.1	2	0.3
41	RNO 91	< 304	< 9.5	< 20	< 3.2	18	5.7	< 15	< 2.3
42	SSTc2d J182813.2	< 32	< 1.0	< 2	< 1.4	< 16	< 5.1	< 5	< 2.9
43	SSTc2d J182849.4	< 480	< 14.5	< 18	< 9.7	< 36	< 11.3	< 20	< 10.7
44	SSTc2d J182901.8	< 224	< 7.0	< 9	< 5.1	< 9	< 3.0	< 6	< 3.2
45	SSTc2d J182914.8	< 48	< 1.5	< 4	< 2.2	< 10	< 3.3	< 4	< 2.2
46	SSTc2d J182916.2	< 288	< 8.9	< 17	< 9.1	< 9	< 3.0	< 4	< 2.2
47	Serp-S68N	152	4.8	5	2.8	< 3	< 0.9	2	1.3
48	EC69	< 56	< 1.7	7	3.8	< 3	< 1.1	4	2.1
49	Serp-SMM4	< 34	< 1.1	3	1.6	< 0.6	< 0.2	20	10.4
50	EC88	< 368	< 11.4	< 5	< 3.0	< 80	< 24.4	< 95	< 50.0
51	Serp-SMM3	< 316	< 9.8	9	5.0	< 3	< 1.0	20	10.3
52	RCrA IRS5	< 296	< 9.2	< 61	< 8.0	< 14	< 4.5	< 21	< 2.7
53	CrA IRS7 A	< 3320	< 102.3	< 150	< 34.5	25	7.9	< 17	< 3.8
54	CrA IRS7 B	< 800	< 25.1	< 46	< 10.2	16	5.0	< 9	< 2.2
55	CrA IRAS32	< 44	< 1.3	< 6	< 1.3	1	0.4	< 1	< 0.2
56	IRAS 23238+7401	< 352	< 10.9	< 7	< 3.6	< 5	< 1.7	< 3	< 1.6

^a100 K is assumed for the warm component and 1000 K for the hot component. The derived column density and mass of the warm component depend strongly on the assumed temperature. A temperature of 150 and 200 K reduces the column density and mass by respectively a factor of ~ 30 and 140. For the hot component 1500 K instead of 1000 K may result in a reduction of column density and mass up to a factor of 10.

^bFor the unresolved emission a source with $r = 50$ AU is assumed to obtain an estimate of the column density.

